Surface Irradiances Consistent with CERES-Derived Top-of-Atmosphere Shortwave and Longwave Irradiances

Seiji Kato and Norman G. Loeb

NASA Langley Research Center, Hampton, Virginia

Fred G. Rose

Science System & Applications Inc., Hampton, Virginia

David R. Doelling

NASA Langley Research Center, Hampton, Virginia

David A. Rutan and Thomas E. Caldwell

Science System & Applications Inc., Lanham, Maryland

Lisan Yu and Robert A. Weller

Woods Hole Oceanographic Institution, Woods Hole, Massachusetts

ABSTRACT

The estimate of surface irradiance on a global scale is possible through radiative transfer calculations using satellite-retrieved surface, cloud, and aerosol properties as input. Computed top-of-atmosphere (TOA) irradiances, however, do not necessarily agree with observation-based values, for example, from the Clouds and the Earth's Radiant Energy System (CERES). This paper presents a method to determine surface irradiances using observational constraints of TOA irradiance from CERES. A Lagrange multiplier procedure is used to objectively adjust inputs based on their uncertainties such that the computed TOA irradiance is consistent with CERES-derived irradiance to within the uncertainty. These input adjustments are then used to determine surface irradiance adjustments. Observations by the Atmospheric Infrared Sounder (AIRS), *Cloud–Aerosol Lidar and Infrared Pathfinder Satellite Observations* (*CALIPSO*), *CloudSat*, and Moderate Resolution Imaging Spectroradiometer (MODIS) that are a part of the NASA A-Train constellation provide the uncertainty estimates. A comparison with surface observations from a number of sites shows that the bias [root-mean-square (RMS) difference] between computed and observed monthly mean irradiances calculated with 10 years of data is 4.7 (13.3) W m^{-2} for downward shortwave and -2.5 (7.1) W m^{-2} for downward longwave irradiances over ocean and -1.7 (7.8) W m^{-2} for downward shortwave and -1.0 (7.6) W m^{-2} for downward longwave irradiances over land. The bias and RMS error for the downward longwave and shortwave irradiances over ocean are decreased from those without constraint. Similarly, the bias and RMS error for downward longwave over land improves, although the constraint does not improve downward shortwave over land. This study demonstrates how synergetic use of multiple instruments (CERES, MODIS, *CALIPSO*, *CloudSat*, AIRS, and geostationary satellites) improves the accuracy of surface irradiance computations.

1. Introduction

The net top-of-atmosphere (TOA) irradiance (radiative flux) is the flux through the upper boundary of the atmospheric column and net surface flux is the flux through the bottom boundary. Once the TOA and surface net flux are averaged for the entire globe and over a year, the difference of the fluxes at the top and bottom boundary determines the global mean atmospheric energy budget. Understanding the change of the atmospheric energy budget is a key element in understanding

Corresponding author address: Seiji Kato, Mail Stop 420, NASA Langley Research Center, Hampton, VA 23681-2199.
E-mail: seiji.kato@nasa.gov

cloud feedback (Stephens 2005). In addition, the change of the atmospheric energy budget is the driver of global mean hydrological cycle change (Stephens 2005; Mitchell et al. 1987; Allen and Ingram 2002; Stephens and Ellis 2008). Furthermore, components of surface fluxes are physically related. For example, the surface net irradiance at a given location over ocean balances with ocean heating, horizontal energy advection through lateral boundaries of the ocean column, and the sum of latent and sensible heat fluxes at the surface.

Unlike TOA irradiances that can be estimated from broadband radiance observations (Loeb et al. 2005), a global estimate of the irradiance at the surface is only possible through radiative transfer calculations. For example, Zhang et al. (1995, 2004) use satellite-derived cloud properties (Rossow and Schiffer 1991, 1999) and temperature and humidity as inputs to compute surface irradiances. Pinker et al. (2003) estimate surface shortwave irradiances using a relationship between atmospheric transmission and TOA albedo (Pinker and Laszlo 1992). Gupta et al. (1999) also use a parameterized approach in computing both shortwave and longwave surface irradiances. L'Ecuyer et al. (2008) and Kato et al. (2011a) take advantage of vertical cloud profiles observed by active sensors to compute surface irradiances. A study by Kato et al. (2011a) shows that integrating active and passive sensor-derived cloud properties significantly improves surface irradiance estimates, especially over polar regions. When observation-based inputs, especially cloud and aerosol properties, are used, computed irradiances are arguably more consistent with observations at the surface than modeled irradiances produced in, for example, general circulation models. The retrieval error in cloud and atmospheric properties used as inputs, however, directly affects the accuracy and stability of computed surface irradiances. In addition, computed TOA irradiances do not necessarily agree with Clouds and the Earth's Radiant Energy System (CERES; Wielicki et al. 1996) derived TOA irradiances (e.g., Rose et al. 2013). In this study, CERES-derived TOA irradiances are used to constrain surface irradiance computations so that computed TOA irradiances are consistent with CERES observations. The CERES-derived TOA irradiances are from the Energy Balanced and Filled (EBAF; Loeb et al. 2009) product. By constraining surface irradiance computations to EBAF TOA irradiance, we extend the consistency from ocean heating and TOA irradiances to surface irradiances, thereby providing improved estimates of the surface radiation budget.

In the following sections, the process to produce a data product containing surface irradiances constrained by CERES observations is discussed. In the constraining process, surface, atmospheric, and cloud properties used as input are adjusted according to their uncertainty, after correction of bias errors. The uncertainty is estimated observationally, utilizing A-Train data, including data from the Atmospheric Infrared Sounder (AIRS; Chahine et al. 2006), *Cloud–Aerosol Lidar and Infrared Pathfinder Satellite Observations* (*CALIPSO*; Winker et al. 2010), *CloudSat* (Stephens et al. 2008), and Moderate Resolution Imaging Spectroradiometer (MODIS). Because the adjustment of inputs depends on their uncertainties, the uncertainty estimate plays a critical role in the process. Accordingly, adjustments to surface irradiances are made by a radiative transfer model together with numerically derived partial derivatives of surface irradiances with respect to surface, cloud, and atmospheric properties. To verify the method, adjusted surface irradiances are compared with observed surface irradiances at a number of surface sites over both land and ocean. If we can establish the agreement of adjusted surface irradiances with observed surface irradiances to within their uncertainty, the agreement achieves closure among inputs, CERES-derived TOA irradiances, and observed surface irradiances.

Section 2 describes the datasets used in producing surface irradiances that are consistent with CERES-derived TOA irradiances. Section 3 provides an overview of the method. Section 4 discusses approximations made in the adjustment process. Section 5 presents the method to derive the uncertainty of cloud and atmospheric properties. Results of the adjustment are discussed in sections 6–12.

2. Datasets

The constrained surface data product (hereinafter EBAF-surface) is based on two CERES data products. Edition 3-lite SYN1deg-Month provides irradiances to be adjusted and EBAF Ed2.6r (Loeb et al. 2009, 2012b) provides the constraint. In addition, two data products from A-Train observations provide uncertainty estimates. The uncertainty of cloud properties derived from MODIS is estimated using the *CALIPSO*, *CloudSat*, CERES, and MODIS (jointly CCCM) edition B1 merged data product (Kato et al. 2010, 2011a). The uncertainty of temperature and humidity profiles is based on AIRS level 3 data (AIRX3STM.005; Chahine et al. 2006).

SYN1deg-Month is a level 3 product and contains gridded monthly mean computed TOA and surface irradiances along with irradiances at three atmospheric pressure levels (70, 200, and 500 hPa). Irradiance computations are made with 1-h temporal and $1° \times 1°$ spatial resolutions. Detailed descriptions of the irradiance

computation method of SYN1deg-Month are given in Kato et al. (2011a). Modeled irradiances included in SYN1deg-Month are computed with cloud properties derived from MODIS and multiple geostationary satellites (Geo). Each Geo instrument is calibrated with MODIS (Doelling et al. 2013). The Ed2 CERES cloud algorithm (Minnis et al. 2011) derives cloud properties (e.g., fraction, optical depth, top height, particle size, and phase) from narrowband radiances measured by MODIS twice a day from March 2000 through August 2002 (*Terra* only) and four times a day after September 2002 (*Terra* plus *Aqua*). The edition 2 two-channel Geo cloud algorithm (Minnis et al. 1994) provides cloud properties (fraction, top height, and daytime optical depth) every 3 h outside the *Terra* and *Aqua* overpass times. Cloud properties are gridded in $1° \times 1°$ spatial grids and interpolated to 1-hourly temporal grids (hour boxes) to fill hour boxes with no retrieved cloud properties. Up to four cloud-top heights (surface to 700 hPa, 700–500 hPa, 500–300 hPa, and <300 hPa) are retained for each hour box within a $1° \times 1°$ grid box. Cloud properties (cloud-top height, optical thickness, particle size, phase, etc.) are kept separately for four cloud types.

Temperature and humidity profiles used in irradiance computations are from the Goddard Earth Observing System (GEOS-4 and 5) Data Assimilation System reanalysis (Bloom et al. 2005; Rienecker et al. 2008). GEOS-4 is used from March 2000 through October 2007, and GEOS-5 is used beginning November 2007. The GEOS-4 and -5 temperature and relative humidity profiles have a temporal resolution of 6 h. Spatially, the profiles are regridded to $1° \times 1°$ maps. Skin temperatures used in the computations are from GEOS-4 and GEOS-5 at a 3-hourly resolution, the native temporal resolution of GEOS-4 skin temperature, although the GEOS-5 product has a higher 1-hourly native resolution available. Six-hourly temperature and humidity profiles and 3-hourly skin temperature are interpolated for each hour box.

Other inputs used in SYN1deg-Month are ozone amount (Yang et al. 2000) and ocean spectral surface albedo from Jin et al. (2004). Broadband land surface albedos are inferred from the clear-sky TOA albedo derived from CERES measurements (Rutan et al. 2009). The diurnal model of clear-sky TOA albedo (Doelling et al. 2013) is used to infer TOA clear-sky albedo away from the CERES observation time. The clear-sky TOA albedo is then used to infer clear-sky surface albedo. Clear-sky surface albedos for the solar zenith angle of 55° are used for all-sky surface albedos. The emissivity of land and ocean surfaces is from Wilber et al. (1999).
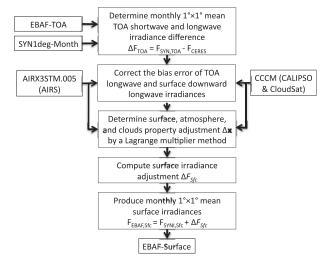

FIG. 1. Flow schematic of the surface irradiance adjustment process to produce the EBAF-surface product.

3. Overview of the EBAF-surface process

The flow diagram in Fig. 1 provides an overview of the process to produce the EBAF-surface data product. To constrain irradiance computations using CERES-derived TOA irradiances, we first determine the difference of the monthly $1° \times 1°$ mean computed and CERES-derived TOA irradiances from SYN1deg-Month and EBAF, respectively. Second, we correct the TOA longwave bias error caused by the upper tropospheric relative humidity error in Global Modeling and Assimilation Office (GMAO) reanalysis using AIRS data. We also correct for the surface downward longwave irradiance bias error that is caused by missing lower clouds in overlapped conditions. This bias correction is based on computed irradiance using *CALIPSO*- and *CloudSat*-derived vertical cloud profiles (Kato et al. 2011a). Third, we use a Lagrange multiplier procedure to determine the perturbation of surface, cloud, and atmospheric properties to match the TOA irradiance difference, assuming that changes applied to the input variables are small relative to respective monthly mean values. Jacobians that are needed to determine surface, cloud, and atmospheric property perturbations, as well as surface irradiance adjustments, are computed separately and used in the Lagrange multiplier procedure. Fourth, we compute the surface irradiance change based on perturbed surface, cloud, and atmospheric properties. Subsequently, the surface irradiance changes are added to $1° \times 1°$ monthly mean SYN1deg-Month irradiances.

4. Approximations in adjusting surface irradiances

To understand approximations in the adjustment process clearly, we write the monthly $1° \times 1°$ gridded mean

TOA irradiance difference from EBAF $\overline{F}_{CERES}$ and SYN1deg-Month $\overline{F}_{SYN}$ and approximate the difference as

$$\Delta\overline{F}_{TOA} = \overline{F}_{SYN,TOA} - \overline{F}_{CERES} = \sum_j \frac{\partial F_{TOA}}{\partial x_j}\Delta\overline{x}_j, \qquad (1)$$

where $\overline{\Delta x}_j$ is the monthly $1° \times 1°$ gridded mean surface, cloud, and atmospheric property adjustments that are determined by the Lagrange multiplier procedure. The bias error caused by the error in upper tropospheric relative humidity is corrected in $\Delta\overline{F}_{TOA}$. Using $\Delta\overline{x}_j$, the surface irradiance adjustments are computed by

$$\Delta\overline{F}_{Sfc} = \sum_j \frac{\partial F_{Sfc}}{\partial x_i}\Delta\overline{x}_j, \qquad (2)$$

after the bias correction is applied to the downward longwave irradiance. The monthly $1° \times 1°$ adjustment given by Eq. (2) is added to the monthly $1° \times 1°$ surface irradiances from SYN1deg-Month,

$$\overline{F}_{EBAF,Sfc} = \overline{F}_{SYN,Sfc} + \Delta\overline{F}_{Sfc}, \qquad (3)$$

to produce the monthly $1° \times 1°$ gridded surface irradiance for EBAF-surface. Because irradiances for SYN1deg-Month are computed with 1-h temporal and $1° \times 1°$ spatial resolutions, the distribution of surface, cloud, and atmospheric properties occurring over the course of the month is treated in the computations. Therefore, the monthly $1° \times 1°$ gridded irradiances from SYN1deg-Month is

$$\overline{F}_{SYN} = \int P(\mathbf{x})F(\mathbf{x})\,d\mathbf{x}, \qquad (4)$$

where $P(\mathbf{x})$ is the probability distribution of TOA or surface irradiances and $\mathbf{x}$ is surface, atmospheric, and cloud properties. We separate $\overline{F}_{SYN}$ into two terms, the irradiance computed from the mean properties and the deviation due to the distribution of atmospheric and cloud properties over the course of the month:

$$\overline{F}_{SYN} = F(\overline{\mathbf{x}}) + \left[\int P(\mathbf{x})F(\mathbf{x})\,d\mathbf{x} - F(\overline{\mathbf{x}})\right], \qquad (5)$$

where the term in the square brackets on the right-hand side is the deviation term.

If we perturb surface, cloud, and atmospheric properties $\mathbf{x}$ at 1 h and $1° \times 1°$ degree resolutions, the monthly $1° \times 1°$ mean irradiance is

$$\overline{F}(\mathbf{x} + \Delta\mathbf{x}) = F(\overline{\mathbf{x}} + \Delta\overline{\mathbf{x}}) + \left[\int P(\mathbf{x} + \Delta\mathbf{x})F(\mathbf{x} + \Delta\mathbf{x})\,dx \right.$$
$$\left. - F(\overline{\mathbf{x}} + \Delta\overline{\mathbf{x}})\right]. \qquad (6)$$

The process described by Eqs. (1)–(3) approximates Eq. (6) by

$$\overline{F}_{EBAF,Sfc}(\mathbf{x} + \Delta\mathbf{x}) = F(\overline{\mathbf{x}}) + \frac{\partial F_{Sfc}}{\partial\mathbf{x}}\Delta\overline{\mathbf{x}}$$
$$+ \left[\int P(\mathbf{x})\,F_{Sfc}(\mathbf{x})\,dx - F_{Sfc}(\overline{\mathbf{x}})\right]. \quad (7)$$

Two approximations by Eq. (7) are 1) neglecting higher-order terms of Taylor's expansions of the first term of the right-hand side of Eq. (6) and 2) neglecting the adjustment applied to the deviation term [i.e. approximating the second term of the right-hand side of Eq. (6) by the third term of the right-hand side of Eq. (7)]. A study by Kato et al. (2011b) indicates that the error by the first approximation is on the order of 10% of the adjustment $\Delta\overline{F}_{Sfc}$. The error by the second approximation is difficult to estimate but it is also expected to be a small fraction of $\Delta\overline{F}_{Sfc}$ because the change of the difference between the mean irradiance $\overline{F}(\mathbf{x})$ and irradiance computed with mean properties $F(\overline{\mathbf{x}})$ by $\Delta\overline{\mathbf{x}}$—that is, $[F(\overline{\mathbf{x}} + \Delta\overline{\mathbf{x}}) - \overline{F}(\mathbf{x} + \Delta\mathbf{x})] - [F(\overline{\mathbf{x}}) - \overline{F}(\mathbf{x})])$—is much smaller than the difference of $F(\overline{\mathbf{x}}) - \overline{F}(\mathbf{x})$. Therefore, the error introduced by these two approximations is small, which is also demonstrated by Loeb et al. (2012a).

5. Input variable uncertainties and surface irradiance adjustments

The Lagrange multiplier approach used in this study is similar to that used in Loeb et al. (2009) and discussed in Rose et al. (2013) in detail. The approach used in this study only uses monthly mean shortwave and longwave irradiances in contrast to the instantaneous TOA shortwave, longwave, and window irradiances discussed in Rose et al. (2013). The detailed adjustment algorithm used in this study is explained in the appendix.

The adjustment determined by the Lagrange multiplier procedure is applied to variables listed in Table 1. One uncertainty value is used for each monthly $1° \times 1°$ grid box for each property listed in Table 1. Note that although four different cloud types are kept in SYN1deg-Month and cloud property uncertainties are derived separately for low, middle, and high clouds, the cloud type–dependent uncertainties are averaged, weighted by the cloud fraction of four cloud types.

TABLE 1. Data source to estimate uncertainty. Note that uppermost cloud-top pressures less than 440 hPa and greater than 680 hPa are defined respectively as high and low clouds. Midclouds are those in between.

Variables	Method and data source	Resolution
Upper tropospheric relative humidity	Difference between AIRS-derived and from reanalysis (GEOS-4 or -5)	Monthly 1° zonal grid. Preadjustment
Surface skin temperature	Difference between AIRS-derived and reanalysis (GEOS-4 or -5)	Monthly 1° zonal grid. Climatology before Sep 2002
Surface air temperature	Difference between AIRS-derived and reanalysis (GEOS-4 or -5)	Monthly 1° zonal grid. Climatology before Sep 2002
Precipitable water	Difference between AIRS-derived and reanalysis (GEOS-4 or -5)	Monthly 1° zonal grid. Climatology before Sep 2002
Aerosol optical thickness	Aeronet/MODIS validation–based estimate	Global land (15%), global ocean (10%) separately
Surface albedo	Estimate	Global land (0.08), global ocean (0.01), global cryosphere (0.08) separately
Cloud fraction	Difference between *CALIPSO*- and *CloudSat*-derived and MODIS-derived values (Kato et al. 2011)	Monthly 1° zonal grid, land ocean separately
Cloud optical thickness	Derived from MODIS by two different cloud algorithms (ED3-beta2 standard and enhanced; Kato et al. 2011)	Monthly 1° zonal grid, land ocean separately, cloud type (high, mid, and low) dependent
Cloud-top height	Difference between *CALIPSO*- and *CloudSat*-derived and MODIS-derived (Kato et al. 2011)	Monthly 1° zonal grid, land ocean separately, cloud type (high, mid, and low) dependent
Cloud-base height	Difference between *CALIPSO*- and *CloudSat*-derived and MODIS-derived (Minnis et al. 2011)	Monthly 1° zonal grid, land ocean separately, cloud type (high, mid, and low) dependent
TOA shortwave irradiance	Estimate of model accuracy	Single global value ($0.5 \ W \ m^{-2}$)
TOA longwave irradiance	Estimate of model accuracy	Single global value ($0.5 \ W \ m^{-2}$)

Because the result of adjustment depends on the uncertainty estimate, it is important to use realistic uncertainty to obtain meaningful irradiance adjustments. For this reason, we use observations to estimate the uncertainty. Table 1 lists the data source of the uncertainty estimate and the subsection below describes the method to estimate the uncertainty of cloud and atmospheric properties, and the uncertainty in the TOA irradiance.

The adjustment of surface irradiances is computed by the surface, cloud, and atmospheric property adjustments multiplied by the partial derivative of the surface irradiance with respect to cloud or atmospheric property [Eq. (2), Jacobian]. Jacobians are numerically derived for each 1° × 1° grid box using its monthly mean cloud and atmospheric properties. To derive partial derivatives with respect to cloud properties, cloud properties for each cloud type (up to four cloud heights) are perturbed equally. The resulting irradiance changes are then averaged, weighted by the cloud fraction of each cloud type.

The adjustment of shortwave irradiance is more complicated than the longwave adjustment because of the distribution of solar zenith angles over a course of the month within a grid box. To account for the solar zenith angle distribution, we compute the distribution of solar zenith angles in each 1° × 1° grid in a month and determine the solar zenith angle that corresponds to the

25% and 75% populations. We then use the two solar zenith angles in deriving partial derivatives numerically and consequently multiplying the partial derivative by the cloud and atmospheric changes. The shortwave irradiance adjustment applied to the monthly mean surface shortwave irradiance for the 1° × 1° is the average of these two values.

The Lagrange multiplier method minimizes changes of the cloud fraction, atmospheric, and cloud properties in adjusting the TOA irradiances. Their adjustments also depend on the uncertainty of TOA irradiances. This approach is suitable for correcting small independent errors in inputs. It does not provide the proper correction, however, if two variables need to be perturbed in an opposite sign to match a small TOA irradiance difference. Suppose, for example, the TOA longwave irradiance needs to increase by a small amount and a large increase of upper tropospheric humidity and even a larger increase of surface temperature that exceeds the TOA longwave reduction by the upper tropospheric humidity are required. This algorithm instead would probably decrease the upper tropospheric humidity or increase the surface temperature or both by a small amount.

To mitigate the weakness of the Lagrange multiplier method, we correct the bias error of upper tropospheric

water vapor amounts using AIRS data. We first compute the monthly upper tropospheric (500 to 200 hPa) relative humidity difference using AIRS level 3 data (AIRX3STM.005) and GEOS-4 or -5 reanalysis. For the time period outside AIRS observations, from March 2000 through August 2002, we use climatological 1° zonal monthly mean upper tropospheric relative humidities derived from the entire AIRS data. Second, we compute the monthly gridded mean TOA irradiance contribution by the upper tropospheric relative humidity by perturbing monthly mean upper tropospheric relative humidity according to the AIRS and GEOS humidity difference. Third, we subtract the irradiance contribution from the TOA irradiance difference between TOA EBAF and computed TOA irradiance from SYN1deg-Month. The residual TOA irradiance differences are used for the correction of other variables using the Lagrange multiplier method. The reason for selecting the upper tropospheric relative humidity for this preadjustment is that it has a smaller diurnal cycle than either near-surface temperature or column-integrated relative humidity so twice daily sampling by AIRS is affected less by the diurnal cycle.

The surface downward longwave irradiance is not well constrained by TOA irradiance. In addition, Kato et al. (2011a) show that the MODIS-derived cloud base (Minnis et al. 2011) is too high because it misses the lower clouds of overlapping clouds. To mitigate this problem, we correct the bias error of the surface downward longwave irradiance in the Lagrange multiplier procedure (see the appendix). The correction is derived from the surface downward irradiance difference computed with and without CALIPSO- and CloudSat-derived cloud profiles (Kato et al. 2011a). A monthly 1° zonal correction is then applied depending on cloud type (low, middle, and high clouds) and surface type (land and ocean).

Cloud, atmospheric property, and TOA irradiance uncertainty

To derive uncertainty of MODIS-derived cloud properties, we use the difference of cloud properties derived from CALIPSO–CloudSat merged cloud profiles (Kato et al. 2010) and from MODIS. The monthly zonal difference of the cloud fraction, cloud-top height, and cloud-base height are computed. To screen thin cloud layers from CALIPSO–CloudSat combined cloud profiles, the optical thickness from the uppermost cloud top is computed by integrating the extinction coefficient derived from CALIPSO. Cloud layers with less than 0.3 cloud optical thickness from the uppermost cloud top are neglected. The cloud property difference then is computed over ocean and land and three different cloud types, high-, middle-, and low-level clouds separately. Following

the International Satellite Cloud Climatology Project (ISCCP; Rossow and Schiffer 1991), we define clouds with uppermost cloud-top pressure less than 440 hPa and greater than 680 hPa, respectively, as high- and low-level clouds. Middle-level clouds (also called midclouds) are those in between. The difference of cloud optical thickness derived from two different cloud algorithms using MODIS radiances is also computed. One cloud algorithm is the edition 3 beta2 CERES cloud algorithm (Minnis et al. 2011). The other one is the "enhanced" cloud algorithm that uses cloud-top height derived from CALIPSO and CloudSat. The detail of the enhanced cloud algorithm is discussed in Kato et al. (2011a). The relative difference of the linearly averaged cloud optical thicknesses derived from standard and enhanced cloud algorithms is used for the uncertainty. A linear mean is used instead of a logarithmic mean because the linear mean weights optically thicker clouds more than thin clouds (compared to the logarithmic mean), further reducing the influence of frequent thin clouds in the CALIPSO cloud mask. Note that to reduce the noise in cloud property uncertainties, the 1° zonal and monthly differences are smoothed by a 5° zonal moving window.

For surface skin temperature, surface air temperature, and precipitable water uncertainties, we use the level 3 AIRS product (AIRX3STM.005) to derive the difference of AIRS-derived values and those from GEOS-4 and -5 for each 1° × 1° grid and each month. Similar to the upper tropospheric relative humidity, we use a climatological monthly mean value derived from the entire AIRS data for the time period outside AIRS observations, from March 2000 through August 2002.

We use a constant value of 0.5 W m^{-2} for all grids for both shortwave and longwave for TOA irradiance uncertainty based on the stability of CERES derived irradiance of approximately 0.5 W m^{-2} per decade (Loeb et al. 2012a). We use all cloud, temperature, humidity, and TOA irradiance differences discussed in this section for s_{c_i}, $\mathbf{s}_v$, and $\mathbf{s}_f$ shown in Eq. (A4). Other sources of uncertainty estimates used in this study are listed in Table 1.

6. Result of TOA and surface modeled irradiance adjustments

Figure 2 shows the mean and root-mean-square (RMS) difference of TOA EBAF and SYN1deg-Month irradiances. Edges of sea ice and mountain regions show a large RMS difference. When computed shortwave and longwave TOA irradiances are adjusted by the Lagrange multiplier, most of the 1° × 1° RMS differences are less than 1.5 W m^{-2} for shortwave and less than 0.7 W m^{-2} for longwave (Fig. 2, bottom). A large
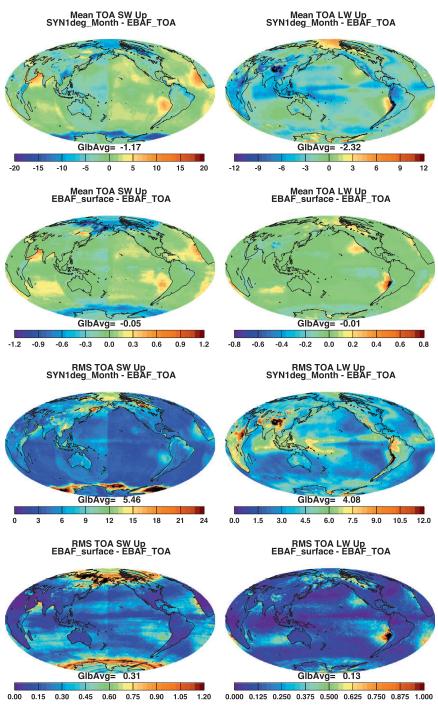
FIG. 2. (top left) Mean of the computed monthly mean irradiance before adjustment (SYN1deg-Month) minus CERES-derived reflected shortwave monthly mean irradiance at TOA from EBAF over $1° × 1°$ grids. (top right) As at left, but for TOA longwave irradiances. (second row). As the top, but the mean of adjusted TOA irradiance (labeled EBAF_surface) minus CERES-derived monthly mean TOA irradiance. (third row) Root-mean-square (RMS) difference of monthly mean modeled all-sky irradiance before the adjustment (SYN1deg-Month) and CERES-derived monthly mean TOA irradiance from EBAF over a $1° × 1°$ grid for reflected shortwave irradiance at TOA. (bottom) RMS difference of adjusted (labeled EBAF_surface) modeled monthly mean irradiances and CERES-derived reflected monthly mean irradiance over a $1° × 1°$ grid for shortwave irradiance at TOA (from TOA EBAF Ed2.6r). The mean and RMS difference are computed using 120 months of data from March 2000 through February 2010. The global mean value shown in the plot is the average of bias for top four plots and RMS for bottom four plots.

difference ($\sim$1.3 W m^{-2}) over the stratocumulus region at the coast of Chile, shown on the right side of the second row of Fig. 2, indicates that adjusting TOA longwave irradiance errors caused by the cloud height error and temperature inversion by this approach is challenging. Figure 3 shows the mean and RMS difference of monthly mean surface irradiance changes (SYN1deg minus EBAF-surface) over 1° × 1° grids caused by the adjustment at TOA. As we discuss in section 9, most adjustments are within the uncertainty of surface irradiances. Note that a line appearing at the date line is caused by artifacts using cloud properties derived from the Multifunctional Transport Satellite (MTSAT) (covering 80° to 180°E), which shows a nonlinear response of its visible detectors (Doelling et al. 2013). Figures 2 and 3 show that the adjustment mitigates artifacts caused by, for example, MTSAT.

Clear-sky surface irradiance adjustment

Clear-sky TOA irradiances included in SYN1deg-Month are derived from 100% clear-sky scenes over a CERES footprints. When 100% clear-sky scenes over a 20-km size footprint do not occur in some regions in some months, SYN1deg-Month sometimes contains a default value. To mitigate this problem, additional clear-sky TOA irradiances are derived using MODIS narrowband radiances averaged over a clear part of a CERES footprint for the EBAF product (Loeb et al. 2009).

While irradiances under clear-sky conditions are computed regardless of the presence of clouds (i.e., clouds are removed from cloudy-sky scenes for clear-sky irradiance computations, hereinafter called "cloud-removed clear-sky irradiance"), which is done in GCMs, EBAF TOA clear-sky irradiances are limited to the cases when a scene is not overcast (Loeb et al. 2009). To use CERES-derived TOA clear-sky irradiances as a constraint of computed irradiances, we therefore need to average computed irradiances weighted by the clear-sky fraction to be consistent with observations (hereinafter called "clear-sky fraction-weighted irradiance"). According to Sohn et al. (2010), who used modeled clouds and atmospheric properties at a 7-km spatial resolution, the difference of two different clear-sky definitions (cloud-removed and clear-sky fraction-weighted irradiances) can reach up to 10 W m^{-2} for the 1° × 1° grid monthly mean TOA longwave irradiance. To constrain by CERES-derived clear-sky irradiances, we use computed surface irradiances under clear sky identified by the CERES cloud algorithm (Ed 2; Minnis et al. 1994, 2011) from SYN1deg-Month and average them weighted by the clear-sky fraction (i.e., the sum of irradiances weighted by the clear-sky fraction divided by the sum of clear-sky

fractions) in the EBAF-surface process. The RMS difference of monthly 1° × 1° gridded mean cloud removed and clear-sky weighted computed TOA irradiances can be greater than 8 W m^{-2} for shortwave and greater than 6 W m^{-2} for longwave (Fig. 4). The difference of shortwave irradiance is caused by the different sampling of cryosphere surface. For example, if snow/sea ice cover and cloud cover are anticorrelated, clear-sky scenes tend to occur where the surface is covered by snow or sea ice. As a result, the clear-sky fraction weighted surface albedo is larger than the surface albedo computed by removing clouds. As pointed out by Sohn et al. (2010), the difference of longwave irradiances is caused by a smaller water vapor amount in clear-sky atmospheres. The spatial pattern in longwave, therefore, resembles that of clouds (i.e., regions of high relative humidity).

Figure 5 shows the RMS difference of monthly 1° × 1° gridded mean cloud removed and clear-sky weighted modeled surface net irradiances. Both clear-sky irradiances used in Fig. 5 are before the adjustment. The RMS differences of surface net shortwave and net longwave irradiances are large over polar regions. The maximum RMS difference is 19 and 15 W m^{-2} for surface net shortwave and net longwave irradiances, respectively. The difference is systematic. Therefore, the RMS difference of annual 1° × 1° gridded mean cloud removed and clear-sky weighted modeled surface net irradiances is nearly the same as the RMS difference computed by monthly mean irradiances except for surface upward shortwave irradiance (Table 2).

Similar to the all-sky adjustments, clear-sky surface irradiances are adjusted using the Lagrange multipliers explained in section 6. We use partial derivatives with respect to atmospheric properties that are derived for clear-sky conditions for clear-sky surface irradiance adjustments.

7. Comparison with surface observations

We compare surface irradiances with surface observations to evaluate whether the adjustment improves the agreement. Because surface observations are made at one point in a grid box while computed irradiances are averaged over a 1° × 1° grid box, irradiances measured at surface sites located in areas not representative of the surface properties of the grid box tend to show a large difference from the irradiance averaged over a 1° × 1° grid box (Kato et al. 2012). For example, the difference of monthly mean downward shortwave and longwave irradiance observed at mountain and coastal sites can be greater than, respectively, 20 and 40 W m^{-2} compared to the monthly gridded values where the surface site is
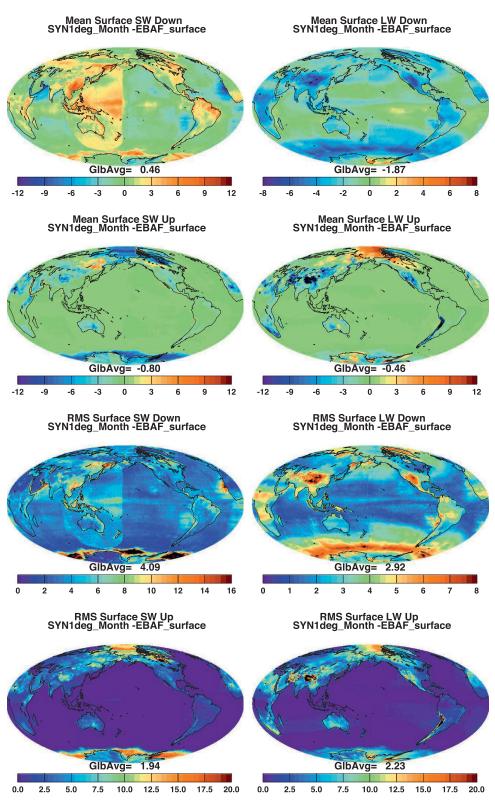
FIG. 3. (top four plots) Mean and (bottom four plots) RMS difference of monthly mean $1° \times 1°$ grid irradiances before (SYN1deg_Month) and after the adjustment (EBAF_surface) for (top left) surface downward shortwave, (bottom left) surface upward shortwave, (top right) surface downward longwave, and (bottom right) surface upward longwave irradiances. Mean and RMS difference are computed using 120 months of data from March 2000 through February 2010.
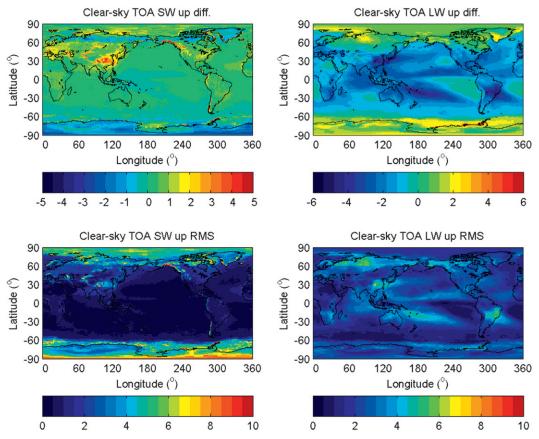
FIG. 4. (top) Difference of modeled clear-sky TOA reflected (left) shortwave and (right) upward longwave irradiance in W m^{-2} defined as clear-sky irradiances computed with clouds removed minus clear-sky fraction weighted irradiances. The differences are computed using 10 years of monthly 1° × 1° gridded mean irradiances from March 2000 through February 2010. (bottom) RMS difference of cloud removed and clear-sky weighted reflected (left) shortwave irradiances and (right) upward longwave irradiances in W m^{-2} computed also using 10 years of monthly 1° × 1° gridded mean irradiances.

located (Kato et al. 2012). Therefore, we select surface sites located in relatively uniform terrain in this study to exclude surface sites that do not represent the grid box.

In addition to surface sites over land, we use surface irradiances observed over ocean by the Improved Meteorological (IMET) system (Colbo and Weller 2009) used on buoys at ocean reference stations. We use shortwave irradiance observations at 71 buoys and longwave irradiance observations at 23 buoys. Locations of land and ocean sites are shown in Fig. 6.

Table 3 summarizes the irradiance bias and RMS differences of EBAF-surface compared with surface observations. For the comparison over land, 15-min averaged observed irradiances computed from original 1-min surface data are used to compute the monthly mean diurnal cycle. The monthly mean diurnal cycle is then used to compute the monthly mean observed irradiance for a given site. This approach minimizes the effect of missing data (Roesch et al. 2010). The mean

and RMS difference decreases from −4.2 (8.4) W m^{-2} for SYN1deg-Month to −1.0 (7.6) W m^{-2} for EBAF-surface for the downward longwave irradiances over land. The downward shortwave irradiance over land is not improved by the adjustment even though the effect of the constraint by TOA irradiance is expected to be larger on the surface shortwave irradiance. A possible reason is that the spatial noise of surface shortwave irradiance is larger than that of surface longwave irradiance, or an explicit treatment of multilayer clouds is necessary. The bias error of the downward shortwave irradiance over ocean, however, decreases from 5.4 to 4.7 W m^{-2}. In addition, the computed downward shortwave irradiance from EBAF-surface agrees better than two other surface radiation products—surface radiation budget (SRB; Stackhouse et al. 2011) and Flushflux (Kratz et al. 2010)—over oceans (Fig. 7). The difference with adjusted downward shortwave irradiance is a factor of 3 smaller than the difference with other two estimates.
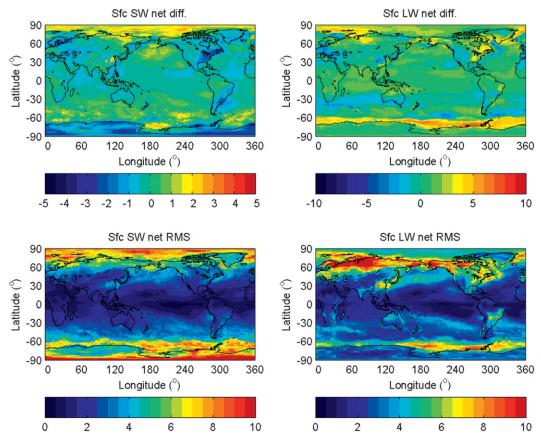
FIG. 5. (top) Difference of (left) modeled clear-sky surface net (downward minus upward) shortwave and (right) surface net longwave irradiances in W m^{-2} defined as clear-sky irradiances computed with clouds removed minus clear-sky fraction weighted irradiances. The differences are computed using 10 years of monthly 1° × 1° gridded mean irradiances from March 2000 through February 2010. (bottom) RMS difference of cloud removed and clear-sky weighted surface net shortwave irradiances on the left and surface net longwave irradiances on the right in W m^{-2} computed also using 10 years of monthly 1° × 1° gridded mean irradiances.

Furthermore, the mean difference of 4.7 W m^{-2} for shortwave and −2.5 W m^{-2} for longwave is within the measurement uncertainty of 5 to 6 W m^{-2} for daily or annual mean downward shortwave and 4 W m^{-2} for daily and annual mean downward longwave irradiances estimated by Colbo and Weller (2009).

8. Global annual mean surface irradiances

After the adjustment of surface irradiances, the global annual mean net surface irradiance is 163 W m^{-2} for shortwave and −54 W m^{-2} for longwave, which leads to the total net surface irradiance of 108 W m^{-2} (Table 4). A better treatment of a diurnal cycle in adjusting surface shortwave irradiance significantly reduces the surface net shortwave irradiance compared to the estimate by Kato et al. (2011a). The global annual mean net atmospheric irradiance is TOA net irradiance minus the net surface irradiance. When we subtract net atmospheric irradiance

under clear-sky conditions from that under all-sky conditions and define it as the cloud radiative effect, it is 4.0 W m^{-2} for shortwave and −3.5 W m^{-2} for longwave. This gives a 0.5 W m^{-2} total cloud radiative effect to the atmosphere. Earlier estimates of the total cloud radiative effect to the atmosphere are shown also to be small

TABLE 2. Global clear-sky irradiance difference in W m^{-2} (cloud removed minus clear-sky fraction weighted irradiances). SW and LW indicate shortwave and longwave, respectively; Sfc indicates surface.

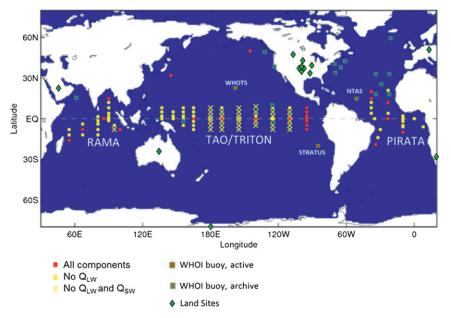|	Monthly			Annual	
	Mean	Std. dev.	RMS	Std. dev.	RMS
TOA SW up	0.24	0.15	0.29	0.03	0.25
TOA LW up	−1.25	0.15	1.26	0.09	1.25
Sfc. SW down	−0.88	0.18	0.90	0.06	0.88
Sfc. SW up	−0.04	0.09	0.10	0.02	0.05
Sfc. LW down	1.63	0.34	1.67	0.07	1.63
Sfc. LW up	0.42	0.33	0.53	0.04	0.42

FIG. 6. Map of surface observation sites used in Table 3.

compared to the cloud radiative effect at TOA and the surface: -0.5 W m^{-2} using ISCCP data estimated by Zhang et al. (2004), 8.0 W m^{-2} using *CloudSat* data estimated by L'Ecuyer et al. (2008), and 2.2 W m^{-2} using CERES SSF estimated by Kato et al. (2008). The range of the all-sky TOA net irradiance is 8.8 W m^{-2} [-2.1 to 6.7 W m^{-2} at the 95% confidence level given by Loeb et al. (2009)] and the uncertainty of the all-sky surface net irradiance is 12 W m^{-2} at the 68% confidence level (Kato et al. 2012). Although clouds affect the meridional gradient of net atmospheric irradiance significantly (Stuhlmann and Smith 1988; Zhang and Rossow 1997; Kato et al. 2008), the atmospheric cloud radiative effect appears to be well within the uncertainty of the

estimate. More rigorous uncertainty estimates by separating bias and random errors are necessary to quantify the uncertainty in the total cloud radiative effect to the atmosphere.

9. Surface irradiances and uncertainties

Our goal is to adjust the $1° \times 1°$ grid monthly mean surface irradiances within their uncertainty. For this purpose, we need to estimate the surface irradiance uncertainty at the grid scale independent of the adjustment. Kato et al. (2012) estimate the uncertainty of surface irradiances for various spatial and temporal scales, including monthly gridded (1° latitude by 1° longitude or

TABLE 3. Summary of monthly mean bias (RMS difference) defined as computed minus observed surface irradiances.

	SYN1deg-Month	EBAF-Surface	SRB	Flashflux
Land[a]				
Shortwave down	0.3 (7.6)	−1.7 (7.8)	−3.4 (9.6)	−4.6 (18.9)[b]
Longwave down	−4.2 (8.6)	−1.0 (7.6)	−0.6 (8.9)	1.0 (7.5)[b]
Ocean[c]				
Shortwave down	5.4 (13.4)	4.7 (13.3)	11.4 (17.7)	14.6 (19.1)
Longwave down	−3.3 (7.1)	−2.5 (7.1)	−1.2 (6.4)	−2.0 (7.6)

[a] Observations at 24 sites from March 2000 through February 2010 are used.

[b] Only 2009 data are used.

[c] Available observations at 23 buoys for longwave [4 Woods Hole Oceanographic Institution (WHOI) buoys, 2 Research Moored Array for African–Asian–Australian Monsoon Analysis and Prediction (RAMA) buoys (McPhaden et al. 2009), 11 Triangle Trans-Ocean Buoy Network (TRITON)/Tropical Atmosphere Ocean (TAO) buoys (McPhaden et al. 1998), 4 Prediction and Research Moored Array in the Tropical Atlantic (PIRATA) buoys (Bourlès et al. 2008), and Kuroshio Extension Observatory (KEO) and Ocean Station Papa (PAPA) buoys from the Pacific Marine Environmental Laboratory (PMEL)] and 71 buoys for shortwave (4 WHOI buoys, 17 PIRATA, 14 RAMA, 34 TRITON/TAO, and KEO+PAPA from PMEL) from March 2000 through February 2010 are used.
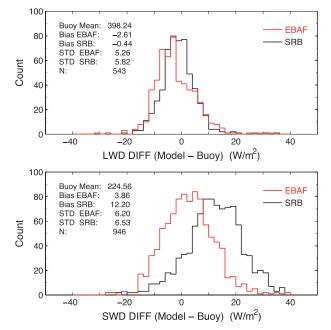
FIG. 7. Histogram of monthly mean downward (top) longwave and (bottom) shortwave irradiance difference; 24 buoy observations from 2001 through 2007 are used. The red line is for EBAF-surface and black line is for SRB surface irradiance (Stackhouse et al. 2011). Numbers shown in the figure are in W m^{-2} except for N, which is the number of monthly observations. Note that biases are different from Table 3 because of different number of samples due to matching EBAF-surface, SRB, and surface observations.

1° latitude by 30° longitude depending on instruments that derive cloud properties used in irradiance computations), monthly zonal, monthly global, and annual global means. The uncertainty estimated by Kato et al. (2012) is summarized in Table 5. Sources of uncertainty included in the estimate are listed in Table 6. In addition to the source of uncertainties considered in Kato et al. (2012), we include the uncertainty of the surface upward longwave irradiance caused by the land surface emissivity uncertainty. A 1% surface emissivity perturbation changes the surface upward longwave irradiance by approximately 0.5 W m^{-2} when the surface temperature is 294 K. Based on this, we estimate the global annual mean uncertainty of 0.5 W m^{-2} (1.5 W m^{-2} × 0.3) due to the surface emissivity uncertainty using the land surface emissivity uncertainty of 3% based on the difference of two datasets given by Zhang et al. (2006) [ISCCP-FD and Wilber et al. (1999)] and a 30% global land cover. Ocean surface emissivity depends on wind speed and temperature. The range of the emissivity change caused by a realistic range of wind speed (Wu and Smith 1997; Hanafin and Minnett 2005) and temperature (Newman et al. 2005) is, however, well less than 1%.

Figure 3 shows that most of the surface irradiance adjustments are within the uncertainty of gridded

TABLE 4. Global annual mean irradiances in W m^{-2} computed using data from March 2000 through February 2010.

	Irradiance component	Ed 2 SYN1deg-Month	Surface EBAF Ed2.6r	EBAF Ed2.6r
TOA	Incoming solar	340	340	340
	LW (all-sky)	237	240	240
	SW (all-sky)	99	100	100
	Net (all-sly)	4.1	0.6	0.6
	LW (clear-sky)	264	266	266
	SW (clear-sky)	53	53	53
	Net (clear-sly)	24	22	22
Surface	LW down (all-sky)	342	344	
	LW up (all-sky)	398	398	
	SW down (all-sky)	187	187	
	SW up (all-sky)	23	24	
	Net (all-sky)	108	108	
	LW down (clear-sky)	314	314	
	LW up (clear-sky)	397	398	
	SW down (clear-sky)	242	243	
	SW up (clear-sky)	29	30	
	Net (clear-sky)	131	130	

Clear-sky irradiances are derived by weighted clear-sky fraction.

irradiances; Approximately 5%, 12%, and 2% of 1° × 1° grid surface downward shortwave, upward shortwave, and upward longwave adjustments, respectively, exceed the uncertainty of gridded irradiance (land+ocean) listed in Table 5. All surface downward longwave irradiance adjustments are less than its monthly gridded uncertainty of 14 W m^{-2}. Therefore, the TOA irradiance constraint by CERES-derived irradiances, which corrects the bias error of modeled TOA irradiances, alters surface irradiances within their uncertainties.

10. Evaluation of surface air temperature and cloud fraction adjustments

As mentioned earlier, the adjustments to atmospheric and cloud properties are determined by their sensitivity to TOA irradiances and uncertainty. The objective of the constraint by CERES-derived irradiance is to adjust surface irradiances rather than obtaining improved cloud and atmospheric properties. We need to check, however, that the magnitude of the adjustment of cloud and atmospheric properties is reasonable.

Figure 8 shows adjustments of surface air temperature, defined as the temperature of a 10-hPa thick layer above the surface pressure, for all-sky and clear-sky conditions. Adjustments under all-sky condition are larger over land but 85% of 1° × 1° gridded values averaged over a year are adjusted less than 1 K. Adjustments within 1 K for clear sky drop to 63% of 1° × 1° gridded values because of adjusting surface air temperature to matching

TABLE 5. Summary of uncertainties in the irradiance computed with satellite-derived cloud and aerosol properties in W m^{-2} (after Kato et al. 2012).

		Mean value	Estimated uncertainty			
			Monthly gridded	Monthly zonal	Monthly global	Annual global
Downward longwave	Ocean+land	345	14	11	7	7
	Ocean	354	12	10	7	7
	Land	329	17	15	8	7
Upward longwave	Ocean+land	398	15	8	3	3
	Ocean	402	13	9	5	5
	Land	394	19	15	5	4
Downward shortwave	Ocean+land	192	10	8	6	4
	Ocean	190	9	8	5	4
	Land	203	12	10	7	5
Upward shortwave	Ocean+land	23	11	3	3	3
	Ocean	12	11	3	3	3
	Land	53	12	8	6	6

clear-sky sampling by CERES. Figure 9 shows the adjustment of cloud fraction. Even though the sensitivity of TOA shortwave irradiance to the cloud fraction is large compared to other cloud properties, the uncertainty in the cloud fraction is relatively small compared to the uncertainty of other cloud properties such as cloud height and cloud optical thickness. As a result, cloud fraction is adjusted very little by the Lagrange multiplier procedure.

TABLE 6. Surface irradiance uncertainty estimate (after Kato et al. 2012).

	Bias error with known sign	Uncertainty	References
Surface downward longwave irradiance			
Cloud-base height	−3.6*		Kato et al. (2011a)
Temporal interpolation	−2.6		Kato et al. (2011a)
Surface temperature		4.5	Kato et al. (2011a)
Precipitable water		5.2	Zhang et al. (2006), Kato et al. (2011a)
Interannual variability		0.8	Kato et al. (2011a)
Overall uncertainty		6.9	
Surface upward longwave irradiance			
Surface skin temperature		3.2	Kato et al. (2012)
Surface emissivity (land only)		0.5	This study
Interannual variability		0.4	Kato et al. (2012)
Uncertainty due to TOA longwave irradiance			
Overall uncertainty		3.3	
Surface downward shortwave irradiance			
Clouds		2.8	Kato et al. (2012)
Aerosol optical thickness**		1.7	Kim and Ramanathan (2008)
Aerosol single scattering albedo**		1.7	Kim and Ramanathan (2008)
Precipitable water**		1.5	Kim and Ramanathan (2008)
Ozone**		0.5	Kim and Ramanathan (2008)
Interannual variability		0.3	Kato et al. (2012)
Uncertainty due to TOA shortwave irradiance			
Overall uncertainty		4.0	
Surface upward shortwave irradiance			
Albedo		3.4	Kato et al. (2012)
Interannual variability		0.1	Kato et al. (2012)
Uncertainty due to TOA shortwave irradiance			
Overall uncertainty		3.4	

* +1.1 W m^{-2} when active sensors are used.

** Surface albedo of 0.12 is used to estimate the downward shortwave uncertainty from the net shortwave uncertainty given by Kim and Ramanathan (2008).
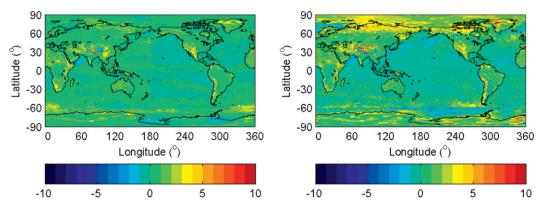
FIG. 8. Surface air temperature, defined as the temperature of a 10-hPa thick layer above the surface pressure, adjustment in K for (left) all-sky and (right) clear-sky conditions. The 1° × 1° gridded values are averaged over one year (2008).

The adjustment of cloud fraction helps reduce the impact of inconsistent geostationary satellite calibrations (Fig. 9, lower left).

The adjustment of cloud fraction and height is effective over the Arctic. Figure 10 shows the probability distribution of the cloud fraction (left) and uppermost cloud-top height (right) difference from those derived from *CALIPSO* and *CloudSat*. It shows that the cloud fraction and cloud-top height differences are reduced with the adjustment.

11. Surface and atmospheric irradiance variability

In this section, we evaluate whether inputs used for EBAF-surface irradiances exhibit essential variabilities such as seasonal variability and land–ocean contrast. In evaluating these variabilities, we primarily check macroscopic cloud properties, cloud fraction in particular, because irradiances are largely affected by cloud property variabilities and cloud vertical profiles observed by *CALIPSO* and *CloudSat* are available.

For the comparison, we use the cloud fraction from three sources: EBAF-surface, which is based on SYN1deg-Month, SSF1deg-Month, and *CALIPSO* and *CloudSat* (from the CCCM data product; Kato et al. 2010). Cloud fraction used in SYN1deg-Month (edition 2) are derived from *Terra* and *Aqua* MODIS and geostationary satellites between 60°N and 60°S and derived from *Terra* and *Aqua* MODIS outside 60°N and 60°S. Cloud fraction used in SSF1deg-Month (edition 2.6) are derived from *Terra* MODIS only. Figure 11 shows seasonal variability of the cloud fraction computed over different regions. The cloud fraction used for EBAF-surface shows seasonal variability and land ocean contrast that agree with those derived from MODIS only (used for Ed2 SSF1deg-Month). In addition, while cloud fraction is biased low compared with *CALIPSO*- and *CloudSat*-derived cloud fraction, the seasonal variability and land ocean contrast of cloud fraction agrees with those derived from *CALIPSO* and *CloudSat* except over the Antarctic. Note that the presence of polar stratospheric clouds (PSC) detected by *CALIPSO* during Antarctic winter
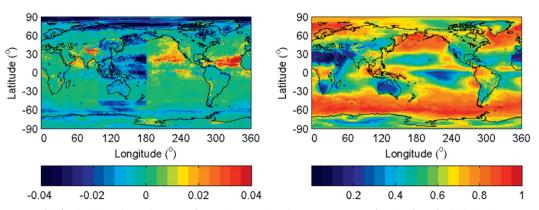

FIG. 9. (left) Cloud fraction adjustment (SYN1deg-Month minus surface EBAF). The 1° × 1° gridded values are averaged over one year (2008). (right) Adjusted cloud fraction (surface EBAF) averaged over 1 year (2008).
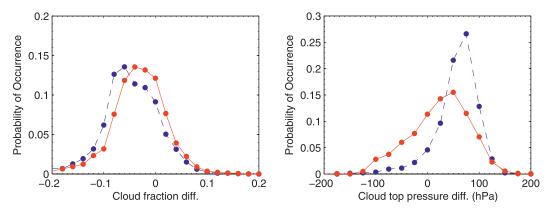
FIG. 10. Probability of occurrence of the (left) cloud fraction difference and (right) effective cloud-top pressure difference. The difference is defined as before adjustment (from SYN1deg-Month, dashed blue line) or after adjustment (from surface EBAF, solid red line) minus values computed from *CALIPSO*- and *CloudSat*-derived cloud profiles. Cloud layers with optical thickness from the uppermost cloud top less than 0.3 are neglected. Data taken over 60° to 83°N and from January through December 2007 are used.

adds a complication to the cloud fraction comparison over Antarctica because screening PSC is not simple (e.g., Pitts et al. 2009; Kato et al. 2010). The cloud fraction computed with (dash-dotted line shown in bottom row in Fig. 11) and without (dotted line shown in bottom row in Fig. 11) clouds present above 12 km south of 60°S makes a large difference in the wintertime cloud fraction.

Table 7 shows the comparison of the standard deviation of deseasonalized anomalies computed from SYN1-deg-Month and EBAF surface. On the one hand, if the adjustment applied to monthly mean irradiance is significantly greater than the monthly anomaly present in the SYN1deg-Month, the adjustment can alter the standard deviation of deseasonalized anomalies. On the other hand, if the adjustment corrects Geo artifacts, for example, the standard deviation of EBAF surface irradiances can be smaller than that of SYN1deg-Month. Table 7 shows that most of the standard deviations of deseasonalized anomalies computed for the globe are equivalent to, and for the tropics are smaller than, the corresponding standard deviation computed using SYN1deg-Month. Table 7 also shows that the standard deviation of global annual anomalies of net atmospheric irradiance is about a half of the standard deviation of the global annual mean precipitation derived from Global Precipitation Climatology Project (GPCP; Adler et al. 2003) data converted to the latent heart flux. Figure 12 shows the spatial difference of the standard deviation of deseasonalized anomalies computed from SYN1deg-Month and surface EBAF. Larger differences occur predominately in polar regions. Off the coast of Antarctica, EBAF-surface reduces the standard deviation of net surface and atmospheric shortwave irradiance by more than 5 W m^{-2} to a value of 5 to 10 W m^{-2} (shown in Fig. 12). It also increases the standard deviation of net surface and

atmospheric longwave irradiances off the coast of Antarctica by about 5 W m^{-2}. A smaller standard deviation of EBAF-surface in the shortwave atmospheric irradiance anomalies is apparent in the western Pacific, which is a result of partly removing MTSAT artifacts.

To further test surface irradiance variability, we use 120 months of 1° × 1° gridded surface shortwave all-sky and clear-sky irradiances to compute cloud radiative effect at the surface and performed a principal component analysis. Figure 13 shows the first and second eigenvectors and principal components (projection of surface shortwave cloud effect anomalies onto the eigenvectors) computed with deseasonalized surface downward shortwave cloud effect (all-sky minus clear-sky irradiances) before and after adjustment. The correlation coefficient between the first principal component and Southern Oscillation index is 0.84. The first principal component computed without the adjustment is similar to that computed with the adjustment (not shown). The second eigenvector computed with adjustment (middle right) is, however, different from that computed without adjustment (bottom right). The second component with the adjustment is not affected by the artifacts of inconsistent geostationary satellite calibrations (e.g., MTSAT covers 80° to 180°E from November 2005 to June 2010).

12. Summary

We developed a method to adjust monthly 1° × 1° gridded computed surface irradiances by constraining computed TOA irradiances to observed TOA irradiances. The SYN1deg-Month product is used as input and TOA irradiances from the CERES EBAF product are used for the constraint. We used the Lagrange multiplier approach to determine cloud and atmospheric
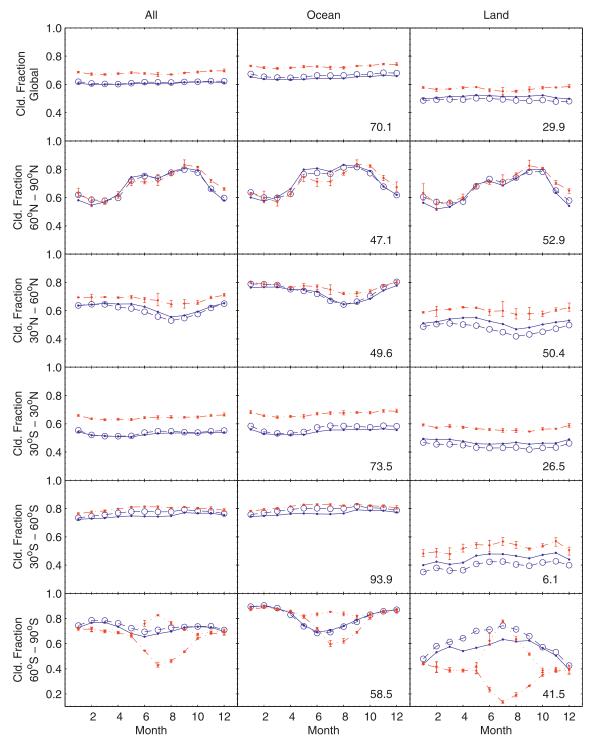
FIG. 11. Monthly mean cloud fraction for, from top to bottom, the globe, Arctic (90°–60°N), Northern Hemisphere midlatitude (60°–30°N), tropics (30°N–30°S), Southern Hemisphere midlatitude (30°–60°S), and Antarctic (60°–90°S). Closed blue circles with solid line are from surface-EBAF (adjusted MODIS- and Geo-derived cloud fraction). Open blue circles with dashed line are from SSF1deg-Month (MODIS-derived cloud fraction). Closed red circles with dash-dotted line are derived from *CALIPSO* and *CloudSat* by neglecting cloud layer with less than 0.3 optical thickness. Note that *CALIPSO* and *CloudSat* observe only over their ground track and from 83°S to 83°N. Three years of data (January 2007–December 2009) are used. Error bars indicate the maximum and minimum values among three months. *CALIPSO* and *CloudSat* cloud fraction derived over the Antarctica with and without including clouds above 12 km are indicated, respectively, by dotted and dash-dotted lines. Numbers in ocean and land plots are their percentage coverage for the corresponding region.

TABLE 7. Standard deviation of global (90°S to 90°N) and tropical (30°S to 30°N) monthly deseasonalized anomalies computed with 10 years of data (March 2000–February 2010) in W m^{-2}.

		Global		Tropics	
	Irradiance	EBAF_sfc.	SYN1deg	EBAF_sfc.	SYN1deg
Surface	SW down	0.77	0.91	1.12	1.31
	SW up	0.29	0.25	0.15	0.13
	SW net	0.69	0.85	1.02	1.22
	LW down	0.80	0.80	1.17	1.17
	LW up	0.65	0.63	0.91	0.93
	LW net	0.63	0.60	0.96	0.99
	SW+LW net	0.62	0.87	1.03	1.29
Atm.	SW+LW net	0.67	0.73	1.08	1.11
TOA EBAF	SW net	0.50		0.78	
	LW up	0.45		0.79	
GPCP global		1.30		—	

property adjustments that correspond to the difference of computed and CERES-derived TOA shortwave and longwave irradiances after the bias error in the TOA longwave due to upper tropospheric relative humidity and in the surface downward longwave irradiance due to low-level cloud cover is corrected. The result of the Lagrange multiplier procedure largely depends on the uncertainty estimate of variables to be adjusted. We estimated the uncertainties almost entirely using observations from *CALIPSO*, *CloudSat*, and AIRS. The adjustment changes surface irradiances within their uncertainty. In addition, the adjustment improves the
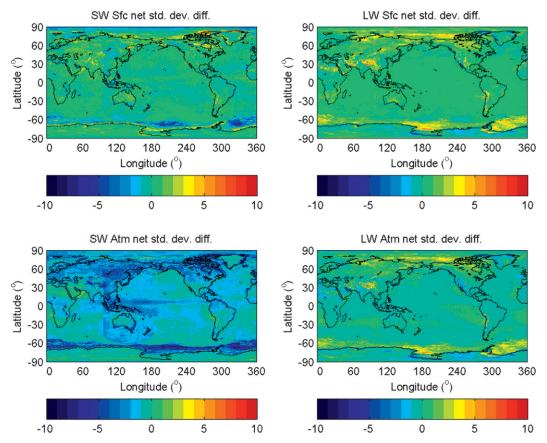

FIG. 12. Difference of standard deviations computed from monthly deseasonalized anomalies over 1° × 1° grids. The difference is defined as surface EBAF (after adjustments) minus SYN1deg-Month (before adjustments). Ten years of data from March 2000 through February 2010 are used.
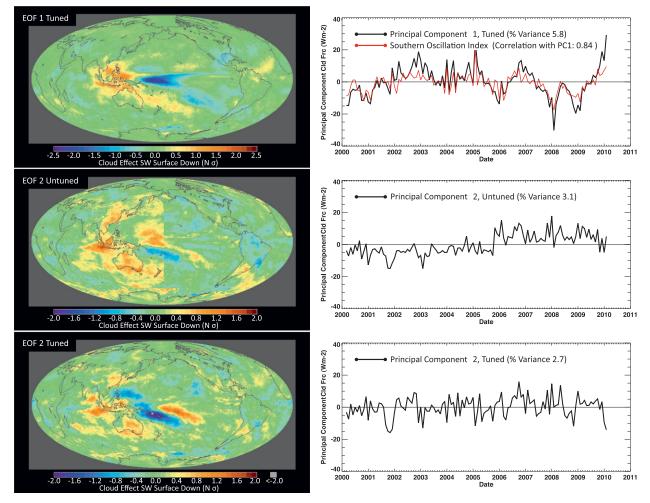
FIG. 13. (top left) First eigenvector computed with deseasonalized surface downward shortwave cloud effect (all-sky minus clear-sky irradiances) after adjustment. The second eigenvector using the downward shortwave cloud effect (middle left) without and (bottom left) with adjustment is also shown. Ten years of monthly $1° \times 1°$ gridded data are used for the analysis. (top right) The first principal component of the deseasonalized surface downward shortwave cloud effect after adjustment with the black line and Southern Oscillation index (multiplied by 4) with the red line. Also shown is the second principal component (middle right) without and (bottom right) with adjustment.

agreement of both surface downward shortwave and longwave with surface observations over ocean and downward longwave over land. The downward shortwave irradiance over land is, however, not improved. Reasons for the improvement compared to the adjustment discussed by Rose et al. (2013), who constrain computations by instantaneous CERES-derived TOA irradiance, are 1) constraining by monthly $1° \times 1°$ mean instead of using instantaneous TOA irradiances that allows us to use a smaller TOA irradiance uncertainty (Table 1) and 2) the use of realistic estimates of surface, cloud, and atmospheric property uncertainties that depend on month and $1° \times 1°$ regions (Table 1). The agreement of computed surface irradiances with observations is remarkable both over ocean and land; the bias (RMS) difference is -1.7 (7.8) W m^{-2} for downward

shortwave and -1.0 (7.6) for downward longwave irradiances over land and 4.7 (13.3) W m^{-2} for downward shortwave and -2.5 (7.1) W m^{-2} for downward longwave irradiances over ocean. The difference of the downward shortwave irradiance with the adjustment over ocean is a factor of 3 smaller than the irradiance estimated by other methods. In addition, artifacts of geostationary satellite-derived cloud properties, often apparent in surface irradiance products, are mostly taken out by the adjustment.

The TOA irradiance constraint developed in this study extends the consistency to the surface radiation budget using 1D radiative transfer theory, anchoring TOA irradiances consistent with ocean heating (i.e., EBAF; Loeb et al. 2009). In deriving such surface irradiances, we used collocated *CALIPSO*, *CloudSat*, MODIS, and CERES

data, as well as level 3 AIRS data, in addition to CERES, MODIS, and geostationary satellites merged data used in CERES data processes. This study demonstrates that merging multiple complimentary instrument observations provides a better surface irradiance estimate than an estimate from fewer measurements. Observations from the A-Train constellation provide a unique opportunity to perform such data integrations.

APPENDIX

Irradiance Adjustment Algorithm

The constraint algorithm used in this study is similar to that discussed in Rose et al. (2013). Descriptions given here closely follow those given in Rose et al. (2013). The difference between CERES-derived irradiance $\mathbf{F}_{\text{CERES}}$ and modeled irradiance $\mathbf{F}_{\text{Model}}$ for a given month and $1° \times 1°$ grid is

$$\Delta \mathbf{F} = \mathbf{F}_{\text{Model}} - \mathbf{F}_{\text{CERES}}, \qquad \text{(A1)}$$

where subscripts "model" and "CERES" indicate computed and observed TOA irradiances. We also include surface upward and downward shortwave and longwave irradiances in $\Delta \mathbf{F}$ so that $\Delta \mathbf{F}$ is a column vector with six elements. All surface components are zero except for the downward longwave irradiance that is set to the monthly zonal cloud type and surface type–dependent bias error (Kato et al. 2011a). The irradiance difference is expressed as

$$\Delta \mathbf{F} = \sum_i [\mathbf{F}_i(s_{c_i} \delta c_i) + C_i \mathbf{a}_i (\mathbf{s}_v^T \delta \mathbf{v})^T] - (\mathbf{s}_f^T \delta \mathbf{f})^T, \qquad \text{(A2)}$$

where $\mathbf{F}_i$ contains the TOA shortwave and longwave irradiance for cloudy or clear-sky (i.e., $i \leq 2$), δc_i is the cloud or clear fraction adjustment divided by the standard deviation (or uncertainty) of cloud fraction s_{c_i}, $\delta \mathbf{v}$ is an $n \times n$ ($n = 9$) square matrix of which off-diagonal elements are all 0 and diagonal elements are cloud and atmospheric variable adjustments such as cloud optical thickness, cloud height, or column water vapor amount (Table 1), and $\mathbf{s}_v$ is the column vector that contains the standard deviation (or uncertainty) of cloud and atmospheric properties. The cloud and atmospheric adjustments in $\delta \mathbf{v}$ are also divided by their standard deviation. Note that δc_i multiplied by s_{c_i} and $\delta \mathbf{v}$ multiplied by $\mathbf{s}_v$ are, therefore, equal to the adjustments. The $6 \times n$ matrix $\mathbf{a}_i$

contains the partial derivative of upward TOA shortwave and longwave irradiance and surface upward and downward shortwave and longwave irradiance with respect to cloud and atmospheric properties. Also, C_i is the cloud fraction and subscript i indicates cloud or clear. For a given $1° \times 1°$ grid box, there are up to four cloud types and one clear-sky condition. But four cloud types are adjusted together so that i is less than or equal to 2. The third term of Eq. (A2) is the residual or tolerance of TOA irradiance differences that are not explained by the first and second term of the right-hand side of Eq. (A2). They are also divided by the uncertainty of CERES-derived shortwave and longwave irradiances. For surface irradiances, the land and cloud type–dependent uncertainties are derived from computed irradiances with and without *CALIPSO* and *CloudSat* cloud profiles. Therefore, diagonal elements of a 6×6 $\delta \mathbf{f}$ are $\Delta \mathbf{F}$ divided by the uncertainties, which is the element of the column vector of $\mathbf{s}_f^T$. We then minimize Z:

$$Z = \sum_i \delta c_i^2 + \text{tr}(\delta \mathbf{v} \delta \mathbf{v}) + \text{tr}(\delta \mathbf{f} \delta \mathbf{f}), \qquad \text{(A3)}$$

where tr indicates the trace of the matrix. An additional constraint is that the sum of cloud and clear factions is equal to unity so that the sum is not altered (i.e., $\sum_{i=1}^2 \delta C_i = 0$). The Lagrange multiplier approach is used to determine the adjustment. If we let Lagrange multipliers λ_0 and $\mathbf{L}^T = [\lambda_1 \lambda_2 \dots \lambda_6]$, we then set up equations by taking the derivative of Y,

$$Y = Z + \lambda_0 \sum_i \delta C_i + \mathbf{L}^T \sum_i \{[\mathbf{F}_i(s_{c_i} \delta c_i) + C_i \mathbf{a}_i (\mathbf{s}_v^T \delta \mathbf{v})^T]$$
$$- (\mathbf{s}_f^T \delta \mathbf{f})^T - \Delta \mathbf{F}\},$$
$$\text{(A4)}$$

with respect to each Lagrange multiplier and with respect to δc_i and each diagonal element of $\delta \mathbf{v}$ and $\delta \mathbf{f}$ and set them equal to zero. The resulting equation can be solved for δc_i and $\delta \mathbf{v}$. The standard deviations s_{c_i}, $\mathbf{s}_v$, and $\mathbf{s}_f$ and irradiance residual $\delta \mathbf{f}$ are specified in advance and used as inputs (Table 1). A larger irradiance uncertainty $\mathbf{s}_f$ gives a smaller adjustment of cloud and atmospheric properties. For given $\mathbf{s}_f$, surface, cloud, and atmospheric properties that have larger uncertainties (s_{c_i} and elements of $\mathbf{s}_v$), larger sensitivity to TOA irradiances (elements of $\mathbf{a}_i$) and larger area coverage C_i are adjusted more than properties with smaller corresponding values.

REFERENCES

Adler, R. F., and Coauthors, 2003: The version-2 Global Precipitation Climatology Project (GPCP) monthly precipitation analysis (1979–present). *J. Hydrometeor.,* **4,** 1147–1167.

Allen, M. R., and W. J. Ingram, 2002: Constraints on future changes in climate and the hydrologic cycle. *Nature,* **419,** 224–232; Corrigendum, **489,** 590.

Bloom, S. A., and Coauthors, 2005: Documentation and validation of the Goddard Earth Observing System (GEOS) data assimilation system, version 4. Technical Report Series on Global Modeling and Data Assimilation, NASA/TM-2005-104606, Vol. 26, 161 pp. [Available online at http://gmao.gsfc.nasa.gov/systems/geos4/.]

Bourlès, B., and Coauthors, 2008: The PIRATA Program: History, accomplishments, and future directions. *Bull. Amer. Meteor. Soc.,* **89,** 1111–1125.

Chahine, M. T., and Coauthors, 2006: AIRS: Improving weather forecasting and providing new data on greenhouse gases. *Bull. Amer. Meteor. Soc.,* **87,** 911–926.

Colbo, K., and R. A. Weller, 2009: Accuracy of the IMET sensor package in the subtropics. *J. Atmos. Oceanic Technol.,* **26,** 1867–1890.

Doelling, D. R., N. Loeb, D. F. Keyes, M. L. Nordeen, D. Morstad, B. A. Wielicki, D. F. Young, and M. Sun, 2013: Geostationary enhanced temporal interpolation for CERES flux products. *J. Atmos. Oceanic Technol.,* in press.

Gupta, S. K., N. A. Ritchey, A. C. Wilber, C. H. Whitlock, G. G. Gibson, and P. W. Stackhouse Jr., 1999: A climatology of surface radiation budget derived from satellite data. *J. Climate,* **12,** 2691–2710.

Hanafin, J. A., and P. J. Minnett, 2005: Measurements of the infrared emissivity of a wind-roughened sea surface. *Appl. Opt.,* **44,** 398–411.

Jin, Z., T. P. Charlock, W. L. Smith Jr., and K. Rutledge, 2004: A parameterization ocean surface albedo. *Geophys. Res. Lett.,* **31,** L22301, doi:10.1029/2004GL021180.

Kato, S., F. G. Rose, D. A. Rutan, and T. P. Charlock, 2008: Cloud effects on meridional atmospheric energy budget estimated from Clouds and the Earth's Radiant Energy System (CERES) data. *J. Climate,* **21,** 4223–4241.

——, S. Sun-Mack, W. F. Miller, F. G. Rose, Y. Chen, P. Minnis, and B. A. Wielicki, 2010: Relationships among cloud occurrence frequency, overlap, and effective thickness derived from CALIPSO and CloudSat merged cloud vertical profiles. *J. Geophys. Res.,* **115,** D00H28, doi:10.1029/2009JD012277.

——, and Coauthors, 2011a: Improvements of top-of-atmosphere and surface irradiance computations with CALIPSO-, CloudSat-, and MODIS-derived cloud and aerosol properties. *J. Geophys. Res.,* **116,** D19209, doi:10.1029/2011JD016050.

——, and Coauthors, 2011b: Detection of atmospheric changes in spatially and temporally averaged infrared spectra observed from space. *J. Climate,* **24,** 6392–6407.

——, N. G. Loeb, D. A. Rutan, F. G. Rose, S. Sun-Mack, W. F. Miller, and Y. Chen, 2012: Uncertainty estimate of surface irradiances computed with MODIS-, CALIPSO-, and CloudSat-derived cloud and aerosol properties. *Surv. Geophys.,* **33,** 395–412, doi:10.1007/s10712-012-9179-x.

Kim, D., and V. Ramanathan, 2008: Solar radiation budget and radiative forcing due to aerosols and clouds. *J. Geophys. Res.,* **113,** D02203, doi:10.1029/2007JD008434.

Kratz, D., S. K. Gupta, A. C. Wilber, and V. E. Sothcott, 2010: Validation of the CERES edition 2B surface-only flux algorithms. *J. Appl. Meteor. Climatol.,* **49,** 164–180.

L'Ecuyer, T. S., N. B. Wood, T. Haladay, G. L. Stephens, and P. W. Stackhouse Jr., 2008: Impact of clouds on atmospheric heating based on the R04 CloudSat fluxes and heating rate data set. *J. Geophys. Res.,* **113,** D00A15, doi:10.1029/2008JD009951.

Loeb, N. G., S. Kato, K. Loukachine, and N. M. Smith, 2005: Angular distribution models for top-of-atmosphere radiative flux estimation from the Clouds and the Earth's Radiant Energy System instrument on the *Terra* satellite. Part I: Methodology. *J. Atmos. Oceanic Technol.,* **22,** 338–351.

——, B. A. Wielicki, D. R. Doelling, G. L. Smith, D. F. Keyes, S. Kato, N. Manalo-Smith, and T. Wong, 2009: Toward optimal closure of the earth's top-of-atmosphere radiation budget. *J. Climate,* **22,** 748–766.

——, S. Kato, W. Su, T. Wong, F. Rose, D. R. Doelling, and J. Norris, 2012a: Advances in understanding top-of-atmosphere radiation variability from satellite observations. *Surv. Geophys.,* **33,** 359–385, doi:10.1007/s10712-012-9175-1.

——, J. M. Lyman, G. C. Johnson, R. P. Allan, D. R. Doelling, T. Wong, B. J. Soden, and G. L. Stephens, 2012b: Observed changes in top-of-the-atmosphere radiation and upper-ocean heating consistent within uncertainty. *Nat. Geosci.,* **5,** 110–113, doi:10.1038/ngeo1375.

McPhaden, M. J., and Coauthors, 1998: The Tropical Ocean–Global Atmosphere observing system: A decade of progress. *J. Geophys. Res.,* **103,** 14 169–14 240.

——, and Coauthors, 2009: RAMA: The Research Moored Array for African–Asian–Australian Monsoon Analysis and Prediction. *Bull. Amer. Meteor. Soc.,* **90,** 459–480.

Minnis, P., W. L. Smith Jr., D. P. Garber, J. K. Ayers, and D. R. Doelling, 1994: Cloud properties derived from GOES-7 for spring 1994 ARM intensive observing period using version 1.0.0 of ARM satellite data analysis program. NASA Reference Publication 1366, 58 pp.

——, and Coauthors, 2011: CERES edition-2 cloud property retrievals using TRMM VIRS and Terra and Aqua MODIS data, Part I: Algorithms. *IEEE Trans. Geosci. Remote Sens.,* **49,** 4374–4400, doi:10.1109/TGRS.2011.2144601.

Mitchell, J. F. B., C. A. Wilson, and W. M. Cunnington, 1987: On CO_2 climate sensitivity and model dependence of results. *Quart. J. Roy. Meteor. Soc.,* **113,** 293–322.

Newman, S. M., J. A. Smith, M. D. Glew, S. M. Rogers, and J. P. Taylor, 2005: Temperature and salinity dependence of sea surface emissivity in the thermal infrared. *Quart. J. Roy. Meteor. Soc.,* **131,** 2539–2557.

Pinker, R. T., and I. Laszlo, 1992: Modeling surface solar irradiance for satellite applications on a global scale. *J. Appl. Meteor.,* **31,** 194–211.

——, and Coauthors, 2003: Surface radiation budget in support of the GEWEX continental-scale international project (GCIP) and GEWEX Americas prediction project (GAPP), including the North American Land Data Assimilation System (NLDAS) project. *J. Geophys. Res.,* **108,** 8804, doi:10.1029/2002JD003301.

Pitts, M. C., L. R. Poole, and L. W. Thomason, 2009: CALIPSO polar stratospheric cloud observations: Second-generation detection algorithm and composition discrimination. *Atmos. Chem. Phys.,* **9,** 7577–7589.

Rienecker, M. M., and Coauthors, 2008: The GOES-5 Data Assimilation System: Documentation of versions 5.0.1, 5.1.0, and 5.2.0. NASA Technical Report Series on Global Modeling and Data Assimilation, Vol. 27, NASA/TM-2008-105606, 97 pp.

Roesch, A., M. Wild, A. Ohmura, E. G. Dutton, C. N. Long, and T. Zhang, 2010: Assessment of BSRN radiation records for the computation of monthly means. *Atmos. Meas. Tech.,* **4,** 339–354, doi:10.5194/amt-4-339-2011.

Rose, F., D. A. Rutan, T. P. Charlock, G. L. Smith, and S. Kato, 2013: An algorithm for the constraining of radiative transfer

calculations to CERES observed broadband top of atmosphere irradiance. *J. Atmos. Oceanic. Technol.,* in press.

Rossow, W. B., and R. A. Schiffer, 1991: ISCCP cloud data products. *Bull. Amer. Meteor. Soc.,* **72,** 2–20.

——, and ——, 1999: Advances in understanding clouds from ISCCP. *Bull. Amer. Meteor. Soc.,* **80,** 2261–2287.

Rutan, D., F. Rose, M. Roman, N. Manalo-Smith, C. Schaaf, and T. Charlock, 2009: Development and assessment of broadband surface albedo from Clouds and the Earth's Radiant Energy System clouds and radiation swath data product. *J. Geophys. Res.,* **114,** D08125, doi:10.1029/2008JD010669.

Sohn, B. J., T. Nakajima, M. Satoh, and H.-S. Jang, 2010: Impact of different definitions of clear-sky flux on the determination of longwave cloud radiative forcing: NICAM simulation results. *Atmos. Chem. Phys.,* **10,** 11 641–11 646, doi:10.5194/acp-10-11641-2010.

Stackhouse, P. W., Jr., S. K. Gupta, S. J. Cox, T. Zhang, J. C. Mikovitz, and L. M. Hinkelman, 2011: The NASA/GEWEX surface radiation budget release 3.0: 24.5-year dataset. *GEWEX News,* No. 21 (1), International GEWEX Project Office, Silver Spring, MD, 10–12.

Stephens, G. L., 2005: Cloud feedbacks in the climate system: A critical review. *J. Climate,* **18,** 237–273.

——, and T. D. Ellis, 2008: Controls of global mean precipitation increases in global warming GCM experiments. *J. Climate,* **21,** 6141–6155.

——, and Coauthors, 2008: CloudSat mission: Performance and early science after the first year of operation. *J. Geophys. Res.,* **113,** D00A18, doi:10.1029/2008JD009982.

Stuhlmann, R., and G. L. Smith, 1988: A study of cloud-generated radiative heating and its generation of available potential energy. Part II: Results for a climatological zonal mean January. *J. Atmos. Sci.,* **45,** 3928–3943.

Wielicki, B. A., B. R. Barkstrom, E. F. Harrison, R. B. Lee III, G. L. Smith, and J. E. Cooper, 1996: Clouds and the Earth's Radiant Energy System (CERES): An Earth observing system. *Bull. Amer. Meteor. Soc.,* **72,** 853–868.

Wilber, A. C., D. P. Kratz, and S. K. Gupta, 1999: Surface emissivity maps for use in satellite retrievals of longwave radiation. NASA Tech. Memo. TP-1999-209362, 30 pp.

Winker, D. M., and Coauthors, 2010: The CALIPSO Mission: A global 3D view of aerosols and clouds. *Bull. Amer. Meteor. Soc.,* **91,** 1211–1229.

Wu, X., and W. L. Smith, 1997: Emissivity of rough sea surface for 8–13 μm: Modeling and verification. *Appl. Opt.,* **36,** 2609–2619.

Yang, S.-K., S. Zhou, and A. J. Miller, cited 2000: SMOBA: A 3-D daily ozone analysis using SBUV/2 and TOVS measurements. [Available online at http://www.cpc.ncep.noaa.gov/products/stratosphere/SMOBA/smoba_doc.shtml.]

Zhang, Y.-C., and W. B. Rossow, 1997: Estimating meridional energy transports by the atmospheric and oceanic general circulations using boundary fluxes. *J. Climate,* **10,** 2358–2373.

——, ——, and A. A. Lacis, 1995: Calculation of surface and top of atmosphere radiative fluxes from physical quantities based on ISCCP data sets: 1. Method and sensitivity to input data uncertainties. *J. Geophys. Res.,* **100,** 1149–1165.

——, ——, ——, V. Oinas, and M. I. Mishchenko, 2004: Calculation of radiative fluxes from the surface to top of atmosphere based on ISCCP and other global data sets: Refinements of the radiative transfer model and the input data. *J. Geophys. Res.,* **109,** D19105, doi:10.1029/2003JD004457.

——, ——, and P. W. Stackhouse Jr., 2006: Comparison of different global information sources used in surface radiative flux calculation: Radiative properties of the surface. *J. Geophys. Res.,* **112,** D01102, doi:10.1029/2005JD007008.